Determination of Orbital Elements of 2002 KL6 via the Method of Gauss

Valentinian Lungu, Anna Khoroshilov, Jason Kim
Team 4, Summer Science Program 2016
New Mexico Institute of Mining and Technology: Frank T. Etscorn Observatory: July 23, 2016

ABSTRACT

Using the Method of Gauss, we performed an orbital determination of the near earth asteroid 2002 KL6. Using the orbital elements gained from this calculation, we then analyzed the properties and inferred the family of asteroid in which 2002 KL6 resides. Using predicted equatorial coordinate data from NASA's Jet Propulsion Laboratory, we used a 0.36 meter, f/11 reflector, C-14 telescope at the Etscorn Observatory (719) to image 2002 KL6 on three separate nights. We also credit Annie Chen, Daniel Michael, and Kathryn Chan for providing a fourth set of images of 2002 KL6 in order to enhance the accuracy of our data through differential correction. After performing astrometric and photometric analyses, we submitted our data to the IAU Minor Planet Center. The astrometric data in the form of equatorial coordinates was also used to determine the unit range vectors from Etscorn Observatory to 2002 KL6 and thus determine the position and velocity vectors of the asteroid at the central observation using the Method of Gauss. These two vectors could then be used to determine the orbital elements of the asteroid. Given that our data suggested that the orbit of 2002 KL6 was entirely outside the Earth's, we can determine that this asteroid belongs to the Amor group of near earth asteroids.

1. INTRODUCTION

Over several weeks, our goal was to image a near-earth asteroid and obtain astrometric and photometric data: that is determine the equatorial coordinates of the object and its observable magnitude. Using positional information for the asteroid at four distinct observations, we were able to determine its orbit using the method of Gauss. Positional and photometric data for 6 data points was also submitted to the IAU Minor Planet Center. Imaging and researching near-earth asteroids is relevant today in context of the determination of their orbits. To date, hundreds of asteroids have been classified as potentially hazardous. It is therefore important to monitor not only those asteroids but also others to detect possible shifts in their orbits that could make them potentially hazardous. The orbital elements calculations required an LSPR (Least Squares Plate Reduction) as well as an Orbital Determination code that was all written in Python independently by all group members.

2. MATERIALS AND METHODS:

1. Data Collection

We used a 0.36 m telescope, f/11 reflector, C-14 telescope at the Etscorn Observatory (Observer Location = 719 on JPL database). The images were taken in three different nights in order to be able to find the orbital elements of 2002 KL6 using the Method of Gauss. Most of the time, we managed to take three or four different sets of visual filter images per night. Along with these, we took Bias and Dark frame calibration images (see FIG 3 and 4). 2002 KL6 was a very bright and fast moving asteroid at the time of our observations, so our exposure time ranged between 30-60 seconds (see FIG. 1). At every observation, we focused the camera on a relatively bright star of apparent magnitude of 4 to 6.

Date	Exposure Time(seconds)
July 27 2016	60
July 5 2016	45
July 9 2016	45
July 18 2016	30

FIG 1. Exposure times on different dates

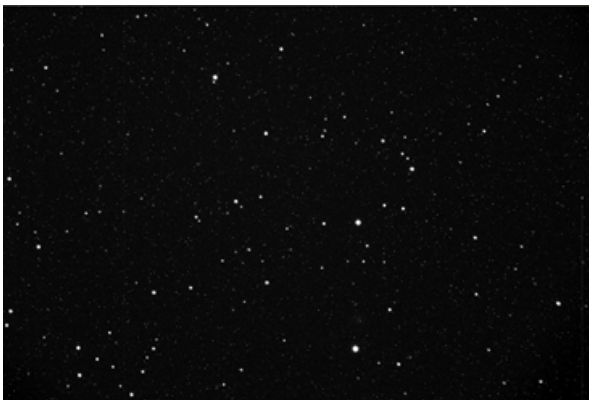

FIG 2. Raw Image in Visual on July 9th

FIG 3. Dark Image on July 9th

FIG 4. Bias Image on July 9th

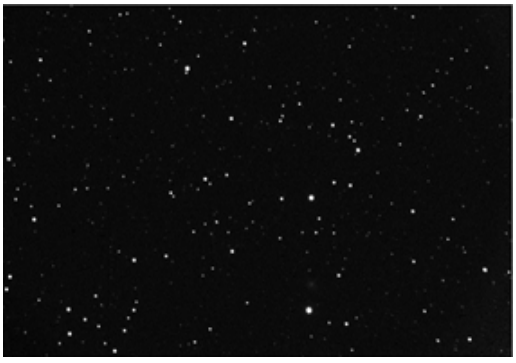

FIG 5. Reduced Image on July 9th

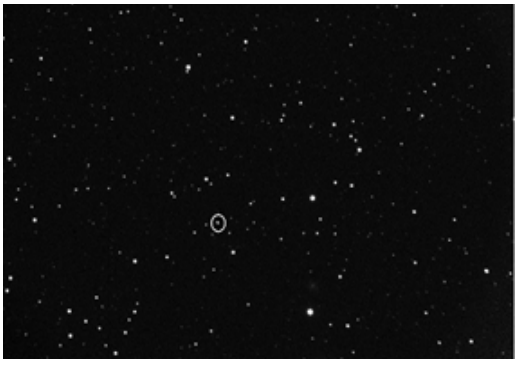

FIG 6. Aligned image with our asteroid (in the circle)

2. Data reductions

We used the CCD Soft software package to reduce and align our images. A blink comparison of our images then revealed our asteroid as it moved with respect to the background stars.

3. Programming analysis

First, all team members wrote centroid programs to help us to find the correct position of a star. A centroid program has for input a pixel coordinate for the approximate center of a star in an image and outputs the real x and y pixel coordinates of the star's center (see FIG. 7). Then, we chose twelve bright stars around our asteroid and noted their Right Ascension and Declination in a .txt file. The LSPR code was then written to take all the data from the file and by using the Method of the Least Squares give a good approximation for equatorial coordinates for our asteroid.

	Coordinates using the Centroiding	
Date of observation(UT time)	X(pixels)	Y(pixels)
2016-06-28 04:19:47.289	502.166676588	458.786892077
2016-06-28 04:39:54.089	484.070091648	418.854653414
2016-07-05 06:21:54.230	492.002194486	499.007269236
2016-07-05 06:32:42.309	498.006446502	526.999863422
2016-07-09 07:34:43.160	466.636344004	464.557361118
2016-07-09 07:49:56.840	502.213682277	513.694536271
2016-07-18 04:31:34.429	486.005884839	327.005700599
2016-07-18 04:40:16.889	443.757229981	291.968085625

FIG 7. The first two columns are the x and y coordinates using the Centroid Code to find the center of our asteroid

4. Method of Gauss

Once we had the equatorial coordinates we were able to start our Orbit Determination (OD) code to find the asteroid's vector position with respect to the Sun and its velocity. We used the Method of Gauss which requires at least three equatorial coordinates for the asteroid, one for each observation. The Method of Gauss returns a final positional and velocity vector for the asteroid for the middle or second observation. A single position and velocity vector is sufficient to determine the entire orbit of an orbiting body using an ephemeris generator code. The Method of Gauss begins with three unit range vectors from the Earth (at Etscorn) to the asteroid (see equation 1). (Note that i refers to the number of the observation: 1, 2, or 3). This information in combination with the Earth to Sun vector which is widely known and can be accurately obtained from NASA's JPL database can be used to calculate the position vector of the asteroid with respect to the Sun (see FIG. 8)

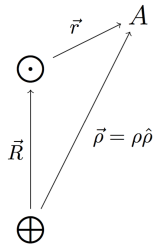

FIG 8. The range vector "rho", Earth to Sun vector "R", and the position vector "r"

$$\hat{\rho}_i = \begin{pmatrix} \cos\alpha_i \cos\delta_i \\ \sin\alpha_i \cos\delta_i \\ \sin\delta_i \end{pmatrix} \tag{1}$$

$$\begin{aligned} D_0 &= \hat{\rho}_1 \cdot (\hat{\rho}_2 \times \hat{\rho}_3)\,, \\ D_{1j} &= (\vec{R}_j \times \hat{\rho}_2) \cdot \hat{\rho}_3\,, \\ D_{2j} &= (\hat{\rho}_1 \times \vec{R}_j) \cdot \hat{\rho}_3\,, \\ D_{3j} &= \hat{\rho}_1 \cdot (\hat{\rho}_2 \times \vec{R}_j)\,. \end{aligned} \tag{2}$$

In order to drastically make the Method of Gauss simpler, specialized Gaussian time units are used instead of standard SI units. Gaussian time units are set up in a way to set the gravitational parameter of the solar system equal to 1. Below the t values refer to the Julian Day numbers of the first, second, and third observations.

$$\begin{aligned} k &= 0.01720209895\,, \\ \mu &= 1\,, \end{aligned} \tag{3}$$

$$\begin{aligned} \tau &\equiv k(t_3 - t_1)\,, \\ \tau_3 &\equiv k(t_3 - t_2)\,, \\ \tau_1 &\equiv k(t_1 - t_2)\,. \end{aligned} \tag{4}$$

The Method of Gauss relies on multiple iterations to become more and more accurate. However to begin the iteration process, an initial guess is needed for the magnitude of the position vector at the central observation. Using Gaussian time units so that the gravitational parameter is equal to 1, we can use the D equations (equation 2) to calculate an approximation of the magnitude of the position vector at the central observation using the scalar equation of Lagrange (equation 10).

$$\begin{aligned} A_1 &= \frac{\tau_3}{\tau}\,, \\ A_3 &= \frac{-\tau_1}{\tau}\,, \end{aligned} \tag{5}$$

$$\begin{aligned} B_1 &= \frac{1}{6} A_1 (\tau^2 - \tau_3^2)\,, \\ B_3 &= \frac{1}{6} A_3 (\tau^2 - \tau_1^2)\,, \end{aligned} \tag{6}$$

$$\begin{aligned} A &= \frac{A_1 D_{21} - D_{22} + A_3 D_{23}}{-D_0}\,, \\ B &= \frac{B_1 D_{21} + B_3 D_{23}}{-D_0}\,, \end{aligned} \tag{7}$$

$$\begin{aligned} E &= -2(\hat{\rho}_2 \cdot \vec{R}_2)\,, \\ F &= R_2^2\,. \end{aligned} \tag{8}$$

$$\begin{aligned} a &= -(A^2 + AE + F)\,, \\ b &= -(2AB + BE)\,, \\ c &= -B^2\,, \end{aligned} \tag{9}$$

$$0 = r_2^8 + a r_2^6 + b r_2^3 + c\,. \tag{10}$$

After choosing the correct root from the solutions to the Scalar Equation of Lagrange, the resulting magnitude of r can be used to make a truncated Taylor Series (equation 12) which allows for the calculation of the magnitude of the range vectors (equation 15) and, through vector subtraction, our first guesses for the position and velocity vector (equation 16).

$$u \equiv \frac{\mu}{r_2^3}\,. \tag{11}$$

$$\begin{aligned} f_i &= 1 - \frac{1}{2}u\tau_i^2\,, \\ g_i &= \tau_i - \frac{1}{6}u\tau_i^3\,. \end{aligned} \tag{12}$$

$$\begin{aligned} C_1 &= \frac{g_3}{f_1 g_3 - f_3 g_1}\,, \\ C_2 &= -1\,, \\ C_3 &= \frac{-g_1}{f_1 g_3 - f_3 g_1}\,, \end{aligned} \tag{13}$$

$$\begin{aligned} d_1 &= \frac{-f_3}{f_1 g_3 - f_3 g_1}\,, \\ d_3 &= \frac{f_1}{f_1 g_3 - f_3 g_1}\,. \end{aligned} \tag{14}$$

$$\rho_i = \frac{C_1 D_{i1} + C_2 D_{i2} + C_3 D_{i3}}{C_i D_0}\,. \tag{15}$$

$$\begin{aligned} \vec{r}_i &= \rho_i \hat{\rho}_i - \vec{R}_i\,. \\ \dot{\vec{r}}_2 &= d_1 \vec{r}_1 + d_3 \vec{r}_3\,. \end{aligned} \tag{16}$$

Once we have our initial guesses for the position and velocity vector, we can use them to make a less-truncated, more accurate Taylor Polynomial for the f and g functions (equation 18). After calculating new Taylor Series Polynomials, equations 13, 14, 15, and 16 are used again to calculate new position and velocity functions. Those, in turn, are used to calculate new f and g functions. This process is repeated until the position and velocity functions reach some tolerance (10 to the power of -12 was used in our case) of precision. To make the Method of Gauss even more accurate, light travel time was taken into account during each iteration and was corrected for.

$$\begin{aligned} u &\equiv \frac{\mu}{r_2^3}\,, \\ z &\equiv \frac{\vec{r}_2 \cdot \dot{\vec{r}}_2}{r_2^2}\,, \\ q &\equiv \frac{\dot{\vec{r}}_2 \cdot \dot{\vec{r}}_2}{r_2^2} - u\,. \end{aligned} \tag{17}$$

$$\begin{aligned} f_i &= 1 - \frac{1}{2}u\tau_i^2 + \frac{1}{2}uz\tau_i^3 + \frac{1}{24}(3uq - 15uz^2 + u^2)\tau_i^4 + \cdots\,, \\ g_i &= \tau_i - \frac{1}{6}u\tau_i^3 + \frac{1}{4}uz\tau_i^4 + \cdots\,. \end{aligned} \tag{18}$$

5. Calculating Orbital Elements

The orbital elements of an orbiting body determine the size and orientation of the orbit as well as the body's position on that orbit at a specific moment in time (see FIG. 9). For a Keplerian orbit where the orbit is an ellipse, the semi-major axis refers to half of the length of the longer axis of the ellipse. The eccentricity is a value between 0 and 1 and is a measure of how elliptical the orbit is. For example, an eccentricity of 0 is a perfect circle and an eccentricity of 1 refers to a parabola. Inclination refers to the angle between the plane of the body's orbit and the plane of the solar system (ecliptic). The longitude of ascending node is the angle between the ascending node and the vernal equinox. The ascending node is the point on the orbit where the object rises above the plane of the ecliptic. The argument of perihelion is the angle along the orbital plane between the ascending node and the perihelion, the point along the orbit where the object approaches closest to the central object, in this case, the Sun. The Mean Anomaly depends on time and is the angle between the object's position along the orbit at a certain time and the perihelion.

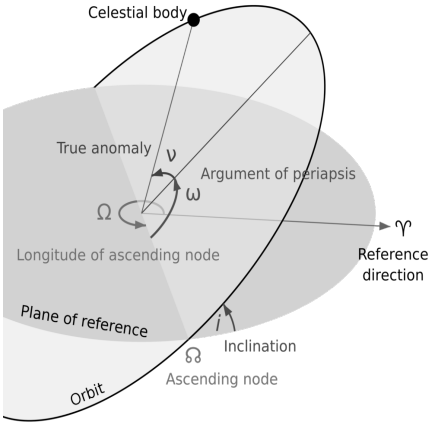

FIG 9. Orbital elements for an orbiting object

The orbital elements can all be calculated based on the position and velocity vector calculated from the Method of Gauss. Note that "a" refers to the semi-major axis, "e" refers to the eccentricity, "i" is the inclination, Capital Omega refers to the longitude of ascending node, lowercase omega refers to argument of perihelion, and M refers to Mean Anomaly. Note that below, mu, or the Gravitational Parameter is still equal to 1. We will also define the vector "h" as the cross product of the position and velocity vectors.

$$\begin{aligned} a &= \left(\frac{2}{r_2} - \frac{\dot{r_2}^2}{\mu}\right)^{-1}, \\ e &= \sqrt{1 - \frac{h^2}{a\mu}}, \\ i &= \cos^{-1}\left(\frac{\vec{h}_z}{h}\right). \end{aligned} \tag{19}$$

$$\begin{aligned} \sin\Omega &= \frac{\vec{h}_x}{h\sin i}, \\ \cos\Omega &= \frac{\vec{h}_y}{h\sin i}. \end{aligned} \tag{20}$$

$$\begin{aligned} \sin(w+f) &= \frac{\vec{r}_{2z}}{r_2\sin i}, \\ \cos(w+f) &= \sec\Omega\left(\frac{\vec{r}_{2x}}{r_2} + \cos i\sin(w+f)\sin\Omega\right). \end{aligned} \tag{21}$$

$$\begin{aligned} \cos f &= \frac{1}{e}\left(\frac{a(1-e^2)}{r_2} - 1\right), \\ \sin f &= \frac{1}{e}\left(\frac{a(1-e^2)}{h}\right)\left(\frac{\vec{r}_2 \cdot \dot{\vec{r}}_2}{r_2}\right). \end{aligned} \tag{22}$$

$$\omega = (\omega + f) - f\,. \tag{23}$$

$$\begin{aligned} n &= \sqrt{\frac{\mu}{a^3}}, \\ \cos E &= \frac{1}{e}\left(1 - \frac{r_2}{a}\right), \\ M_2 &= E - e\sin E\,, \end{aligned} \tag{24}$$

To improve our determined calculations for the orbital elements, we used a differential correction based on the O-C, or observed minus calculated, values for right ascension and declination. In other words, we used the calculated orbital elements to calculate the equatorial coordinates that we started this entire process with and used the difference between the observed and calculated equatorial coordinates to correct our position and velocity vectors. In order to do that we calculated all the numerical partial derivatives for RA and DEC with respect to the x, y, z coordinates and the x, y, z components of the velocity. We summed them up and solved a Jacobian matrix (equation 25). Differential corrections require four observations total. With final orbital elements after both light travel time correction and differential correction, we also included a visual simulation of the asteroid (see FIG. 10).

$$\begin{pmatrix} \sum \Delta\alpha_i \frac{\partial \alpha_i}{\partial x} \\ \sum \Delta\alpha_i \frac{\partial \alpha_i}{\partial y} \\ \sum \Delta\alpha_i \frac{\partial \alpha_i}{\partial z} \\ \sum \Delta\alpha_i \frac{\partial \alpha_i}{\partial \dot{x}} \\ \sum \Delta\alpha_i \frac{\partial \alpha_i}{\partial \dot{y}} \\ \sum \Delta\alpha_i \frac{\partial \alpha_i}{\partial \dot{z}} \end{pmatrix} = \begin{pmatrix} (\frac{\partial \alpha_i}{\partial x})^2 & \frac{\partial \alpha_i}{\partial x}\frac{\partial \alpha_i}{\partial y} & \frac{\partial \alpha_i}{\partial x}\frac{\partial \alpha_i}{\partial z} & \frac{\partial \alpha_i}{\partial x}\frac{\partial \alpha_i}{\partial \dot{x}} & \frac{\partial \alpha_i}{\partial x}\frac{\partial \alpha_i}{\partial \dot{y}} & \frac{\partial \alpha_i}{\partial x}\frac{\partial \alpha_i}{\partial \dot{z}} \\ \frac{\partial \alpha_i}{\partial y}\frac{\partial \alpha_i}{\partial x} & (\frac{\partial \alpha_i}{\partial y})^2 & \frac{\partial \alpha_i}{\partial y}\frac{\partial \alpha_i}{\partial z} & \frac{\partial \alpha_i}{\partial y}\frac{\partial \alpha_i}{\partial \dot{x}} & \frac{\partial \alpha_i}{\partial y}\frac{\partial \alpha_i}{\partial \dot{y}} & \frac{\partial \alpha_i}{\partial y}\frac{\partial \alpha_i}{\partial \dot{z}} \\ \frac{\partial \alpha_i}{\partial z}\frac{\partial \alpha_i}{\partial x} & \frac{\partial \alpha_i}{\partial z}\frac{\partial \alpha_i}{\partial y} & (\frac{\partial \alpha_i}{\partial z})^2 & \frac{\partial \alpha_i}{\partial z}\frac{\partial \alpha_i}{\partial \dot{x}} & \frac{\partial \alpha_i}{\partial z}\frac{\partial \alpha_i}{\partial \dot{y}} & \frac{\partial \alpha_i}{\partial z}\frac{\partial \alpha_i}{\partial \dot{z}} \\ \frac{\partial \alpha_i}{\partial \dot{x}}\frac{\partial \alpha_i}{\partial x} & \frac{\partial \alpha_i}{\partial \dot{x}}\frac{\partial \alpha_i}{\partial y} & \frac{\partial \alpha_i}{\partial \dot{x}}\frac{\partial \alpha_i}{\partial z} & (\frac{\partial \alpha_i}{\partial \dot{x}})^2 & \frac{\partial \alpha_i}{\partial \dot{x}}\frac{\partial \alpha_i}{\partial \dot{y}} & \frac{\partial \alpha_i}{\partial \dot{x}}\frac{\partial \alpha_i}{\partial \dot{z}} \\ \frac{\partial \alpha_i}{\partial \dot{y}}\frac{\partial \alpha_i}{\partial x} & \frac{\partial \alpha_i}{\partial \dot{y}}\frac{\partial \alpha_i}{\partial y} & \frac{\partial \alpha_i}{\partial \dot{y}}\frac{\partial \alpha_i}{\partial z} & \frac{\partial \alpha_i}{\partial \dot{y}}\frac{\partial \alpha_i}{\partial \dot{x}} & (\frac{\partial \alpha_i}{\partial \dot{y}})^2 & \frac{\partial \alpha_i}{\partial \dot{y}}\frac{\partial \alpha_i}{\partial \dot{z}} \\ \frac{\partial \alpha_i}{\partial \dot{z}}\frac{\partial \alpha_i}{\partial x} & \frac{\partial \alpha_i}{\partial \dot{z}}\frac{\partial \alpha_i}{\partial y} & \frac{\partial \alpha_i}{\partial \dot{z}}\frac{\partial \alpha_i}{\partial z} & \frac{\partial \alpha_i}{\partial \dot{z}}\frac{\partial \alpha_i}{\partial \dot{x}} & \frac{\partial \alpha_i}{\partial \dot{z}}\frac{\partial \alpha_i}{\partial \dot{y}} & (\frac{\partial \alpha_i}{\partial \dot{z}})^2 \end{pmatrix} \begin{pmatrix} \Delta x \\ \Delta y \\ \Delta z \\ \Delta \dot{x} \\ \Delta \dot{y} \\ \Delta \dot{z} \end{pmatrix} \tag{25}$$

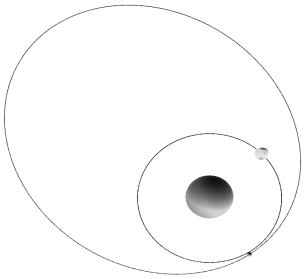

FIG 10. Visual simulation of the asteroid 2002 KL6 with the Sun and Earth.

3. DATA AND ANALYSIS

Date/Time (UT) of Observation	Observing Conditions	Astrometric Data	Apparent Magnitude (V)	Signal to Noise Ratio
2016-06-18 04:19:47.289	Completely clear, high image quality, asteroid observed in raw images. Average sky magnitude 24.7.	RA=17:01:49.02+/-0.369 seconds Dec=+03:51:40.56+/-3.530"	14.5	66.04699
2016-06-28 04:39:54.089		RA=17:01:49.02+/-0.369 seconds Dec=+03:51:40.56+/-3.530"	14.5	75.52374
2016-07-05 06:21:54.230	Completely clear, high image quality, asteroid observed in raw images. Average sky magnitude 24.1.	RA=17:24:53.97+/-0.035 seconds Dec=+12:17:14.01+/-0.361"	13.9	81.41666
2016-07-05 06:32:42.309		RA=17:24:54.59+/-0.035 seconds Dec=+12:17:49.74+/-0.361"	13.9	79.36655
2016-07-09 07:34:43.160	Completely clear, high image quality. Asteroid observed in raw images. Average sky magnitude 24.3.	RA=17:46:01.32+/-0.201 seconds Dec=+18:34:13.93+/-1.266"	13.8	96.07016
2016-07-09 07:49:56.840		RA=17:46:04.68+/-0.201 seconds Dec=+18:35:15.50+/-1.266"	13.9	84.11759
2016-07-18 04:31:34.429	Somewhat cloudy. Some asteroid images taken. Mostly calibration images taken.	RA=19:10:23.14+/-0.130 seconds Dec=+35:39:34.17+/-0.267"	13.2	-
2016-07-18 04:40:16.889		RA=19:10:27.68+/-0.130 Dec=35:40:17.57+/-0.267	13.4	-

FIG 11. A table of all observations and images used to determine the orbit of 2002 KL6. Credits go to Annie Chen, Daniel Michael, and Kathryn Chan for providing the images used for the 2016-07-18 data set.

The raw astrometric data obtained from our images was used to obtain the minimum three unit range vectors from the Earth at Etscorn to 2002 KL6. From there, along with known Earth (at Etscorn) to Sun vectors at the times of our observations obtained from NASA's Jet Propulsion Laboratory Horizons Web interface, we were able to use the Method of Gauss to obtain the orbital elements of 2002 KL6 (see Materials and Methods).

	Semi-Major Axis	Eccentricity	Inclination	Longitude of Ascending Node	Argument of Perihelion	Mean Anomaly
Kim	2.27626064 +/-0.00607207987 528	0.54233571 +/-0.0011933 8180902	3.21149667 +/-0.006543 18274433	213.42193231 +/-0.0459394049274	97.90400853 +/-0.05108299 8555	358.736165 35 +/-0.007517 94816129
Lungu	2.30051161346 +/-0.01550040083 07	0.547062481 865 +/-0.0030208 472592	3.23219604 657 +/-0.015705 8077386	213.501217232 +/-0.0511635142763	97.822497805 +/-0.05272580 76492	358.831954 875 +/-0.005612 748
Khoroshilov	2.2899866278309 986 +/-0.02855514002 44	0.544969763 15472356 +/-0.0056957 6754964	3.21476432 51186975 +/-0.028810 2909174	213.5083722022433 +/-0.0671482788363	97.703932096 0227 +/-0.06596360 87679	359.018313 559 +/-0.024408 81

FIG 12. All orbital elements independently calculated by all team members. Semi-major axis is in AU, eccentricity is unitless, and the rest are in degrees. Note that Mean Anomaly is for July 27 at 9:00:00 UT (JD: 2457596.875)

The observational data that we obtained was able to converge using the Method of Gauss to yield the orbital elements for 2002 KL6 as seen in FIG 12. We also used our calculated orbital elements to cross check accuracy with our joint team (Zhengdong Wang, Neha Kumar, Arian Mansur) that collected data on the same asteroid (see FIG. 13). With our orbital elements we were able to generate the right ascension and declination coordinates at the times the other team observed the asteroid. Below, we present the observed minus calculated results, where the observed data was from our joint team and the calculated data was from our orbital elements. With these relatively low values, we are confident in the accuracy of our orbital elements, especially since they match closely with data acquired from an entirely separate group.

	O-C Right Ascension	O-C Declination
2016 06 30 03:54:27	Kim: -0.00533224365012	Kim: -0.00127501211926
	Lungu: -0.000396664143466	Lungu: 0.0248870344197
	Khoroshilov: 0.0305589762036	Khoroshilov: 0.00761792718488
2016 07 06 05:44:38	Kim: -0.00480505661102	Kim: -0.000673233849533
	Lungu: -0.00316794198909	Lungu: 0.0270497116734
	Khoroshilov: -0.0213704611405	Khoroshilov: -0.0050990102802
2016 07 18 04:45:36	Kim: -0.116802616982	Kim: -0.0397416373458
	Lungu: -0.128665498102	Lungu: -0.0179017115522
	Khoroshilov: -0.350298699784	Khoroshilov: -0.0519532932774
2016 07 12 05:34:01	Kim: -0.00355249895699	Kim: -0.000862917233867
	Lungu: -0.00720374267524	Lungu: 0.0253920731756
	Khoroshilov: -0.106901939059	Khoroshilov: -0.0226075494712

FIG 13. Observed minus Calculated values in degrees for our calculated right ascension and declination coordinates and observed coordinates from Wang et al. (2016)

All values presented here were calculated after a differential correction process. In order to assess the effectiveness of this correction, we calculated observed minus calculated values before and after the differential correction. Given that the O-C values became lower after differential correction, the differential correction was successful in increasing accuracy.

	Before	After
Kim	0.006398954	0.001848
Lungu	0.018665663	0.001427
Khoroshilov	1.103597538	0.775469

FIG 14. Observed minus Calculated rms values for right ascension and declination in degrees before and after differential correction

From the orbital elements as well as the simulation shown above, we can determine that our asteroid is within the Amors group of near earth asteroids, meaning that its orbit is entirely outside of that of Earth. It must be noted that predicted positions of the asteroid suggested that it would be moving rather quickly across the sky during our window of observation. This was later confirmed by the fact that our asteroid was very near perihelion at the time of observation, thus moving at top speeds according to Kepler's Second Law. Thus, astrometric data had acceptable but non-ideal uncertainties (see FIG. 12). However, we felt relatively confident in the usage of our data given that our observed equatorial coordinates matched closely with predicted positions. Since 2002 KL6 was near perihelion, it made a relatively close approach to Earth, leading to very low magnitudes (high brightness) compared to many Near-Earth Asteroids (see FIG 11).

4. CONCLUSION

Given the rather low uncertainty values for our orbital elements, we are certain that our calculations for the orbital elements are rather accurate. Our highest uncertainty was for one of our calculations for longitude of ascending node which was +/-0.0671482788363 while we were able to achieve down to +/-0.00119338180902 for eccentricity. Limited telescope time presented us with some unavoidable challenges including an asteroid that was incredibly fast compared to other observed asteroids in the night sky. The fact that 2002 KL6 was very near its perihelion explained this abnormality as well as the other interesting, but helpful oddity that the asteroid was very bright with a low apparent magnitude. Frequent cloud cover also hampered progress, photometric calculations, and seeing conditions. Other error sources could have been the omission of accounting for curvature when determining LSPR, which was a linear fit calculation. The choice of reference stars for both astrometry and photometry, as well as differences in Python programs between team members which may have led to slightly different rounding errors. For future reference and as a suggestion to any subsequent groups observing such a fast and bright asteroid, in determining exposure times, it is useful to calculate ideal exposure times, taking into account seeing conditions, binning, and sky motion.

Though 2002 KL6 did come somewhat close to the Earth this summer, our orbit determination was able to determine that as an Amor asteroid, 2002 KL6 poses little threat to Earth. A more detailed long-term simulation, which may be described in a later paper, was conducted on the scale of hundreds of thousands of years which predicted that 2002 KL6 will mostly likely eventually fall into the Sun, though the possibilities of being shot out of the solar system or impacting Venus do exist. In the short term, cases like 2002 KL6 are useful in conducting further research on the formation of the solar system and answering questions on how exactly near-Earth asteroids left the main belt and why objects with greater mass seem to have developed less-eccentric orbits.

5. REFERENCES

1) R. Widenhorn, M. Blouke, A. Weber, E. Bodegom, Temperature Dependence of Dark Current in a CCD, 2002
2) Z. Wang, A. Mansur, and N. Kumar, Determination 2002 KL6, 9, 2016

6. APPENDICES

COD 719
CON A. W. Rengstorf
CON [adamwr@pnw.edu]
OBS V. Lungu, A. Khoroshilov, J. Kim
MEA V. Lungu, A. Khoroshilov, J. Kim
TEL 0.36-m f/11 reflector + CCD
NET NOMAD
BND V
NUM 6
ACK Team 4 - 2002 KL6

F4244	C2016 06 28.18040 17 01 49.02 +03 51 40.5	14.5 V	719
F4244	C2016 06 28.19437 17 01 50.73 +03 52 31.2	14.5 V	719
F4244	C2016 07 05.26521 17 24 53.97 +12 17 14.0	13.9 V	719
F4244	C2016 07 05.27271 17 24 54.59 +12 17 49.7	13.9 V	719
F4244	C2016 07 09.31527 17 46 01.32 +18 34 13.9	13.8 V	719
F4244	C2016 07 09.32635 17 46 04.68 +18 35 15.5	13.9 V	719

FIG 11. The data submitted to the IAU Minor Planet Center

Temperature and Time Dependencies of Darks and Biases

1. DATA COLLECTION STRATEGY AND METHODOLOGY

Data was collected over the course of three observations with all of the time-dependent darks collected simultaneously on July 9th and the biases collected on the 14th and 18th together with the temperature-dependent darks. Data collection was structured as to minimize the amount of necessary shifts in temperature. Temperatures were decreased from either or 20 or 17 ℃ by 3° each time, while dark times started at 5s and were doubled until 160s. Five images per setting were taken and averaged before computing results. In addition, CCD Soft was used to reduce the darks before computations (biases of same temperature were used). Regression analysis and error computation were performed in Python.

2. EXPECTED RESULTS

a. Temperature Dependent Biases

The biases account for the difference in excitations between pixels. These differences are not expected to change with temperature so the line of best fit is expected to have a slope close to 0: in other words, its uncertainty range should enclose the 0 value.

b. Time Dependent Darks

With time, it is expected that more thermal electrons be promoted so the total pixel count will increase. The rate of electron promotion is expected to be constant (time does not affect "pixel-conditions" and nothing else changes). From this it can be extrapolated that the pixel count will increase linearly with time.

c. Temperature Dependent Darks

As temperature increases, the number of thermally promoted electrons per second is expected to increase. It is expected that the average pixel count per second will increase exponentially with time and follow the Arrhenius equation (Widenhorn et al, 2002).

3. MEASURED RESULTS

1. TEMPERATURE-DEPENDENT BIASES

First, we took all of the data and applied the Method of Least Squares. The graph obtained is below.

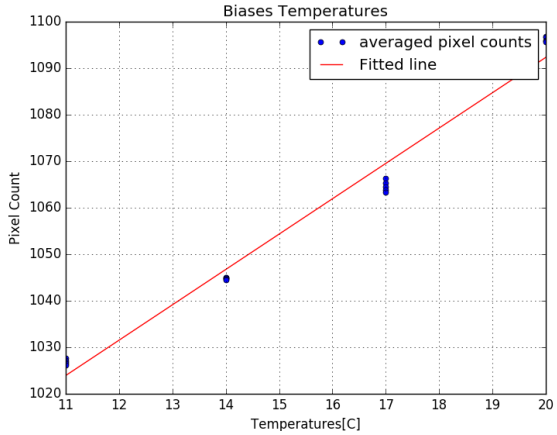

As it can be seen, we have 5 data points for each temperature.

Because we introduce a higher uncertainty, we will average each five data points and then apply the Method of Least Squares. This gives the graph below.

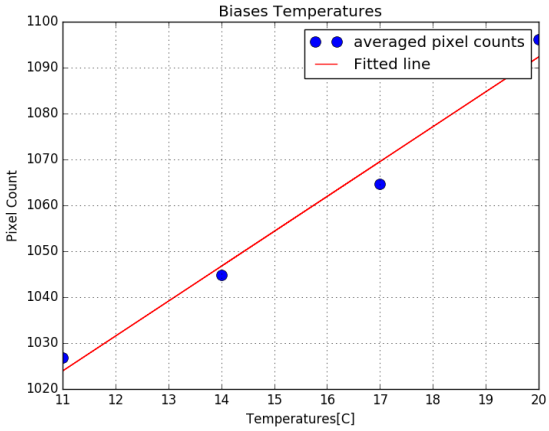

b= 7.60107
a=940.31045
The uncertainties from the method:
Sigma(a)= 60.85793
Sigma(b)= 3.837498

However, we can find a better fitting function for our points. If we choose a quadratic function the graph would change.

As we can see from the graph and best fit line, since sigma for the b-value uncertainty is less than the b-value and thus the slope cannot be 0, we must reject the null hypothesis that biases are independent of time. Although theoretically they would be, and we see in the graph that the sloe is very small, because we cannot technically have a 0s exposure time, a bit of dark current will be incorporated in the biases.

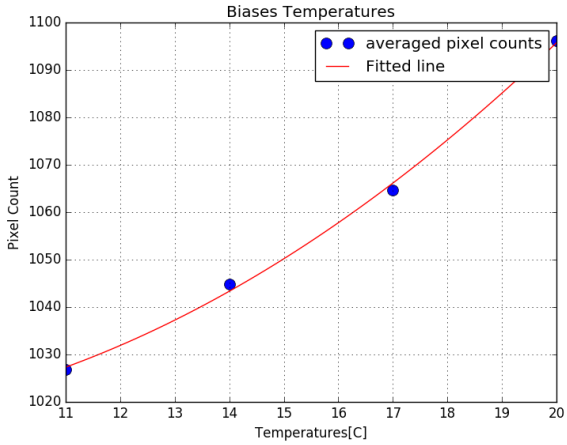

2. TIME-DEPENDENT DARKS

We do the same thing as we did before with the bias pictures. We consider the regression line:

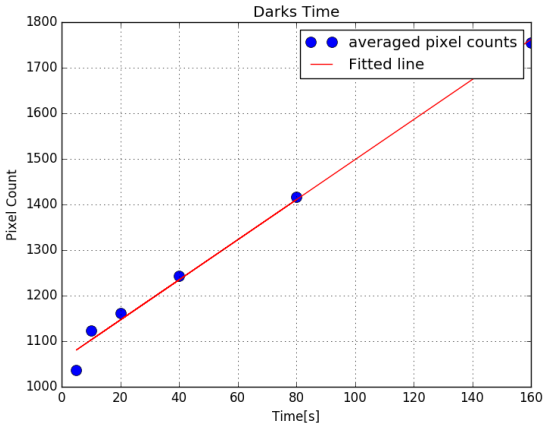

b = 4.39582
a = 1058.60150
The uncertainties from the method:
Sigma(a) = 135.90679
Sigma(b) = 1.80210

As it can be seen, the linear regression line approximates our data pretty well.

3. TEMPERATURE-DEPENDENT DARKS

A first graph of the average-pixel-count-per-second showed the data to take on an exponential form with few outliers, suggesting that it may follow the Arrhenius Principle. To test this, a linear regression was fitted to a modified version of the data - taking a natural logarithm of the average pixel count and the inverse of the temperature.

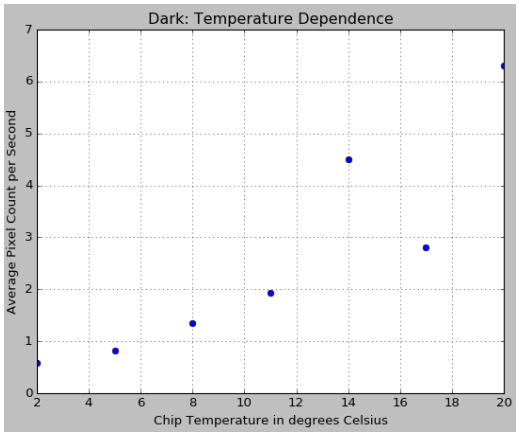

FIG 1. Initial Data Graph

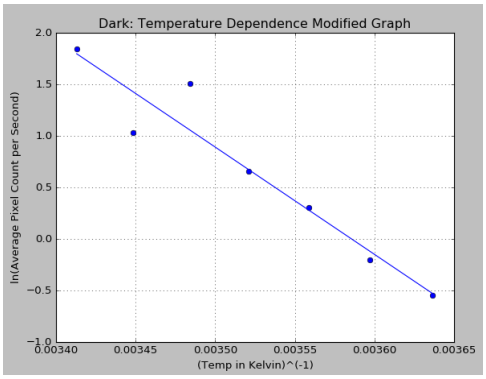

FIG 2. Final Data Graph

b= -10409.4150597
a=37.32397414
The uncertainties from the method:
sigma(a) = 3.7956
sigma(b) =1073.4651

From the linear fit equation b= -10409.4150597; a=37.32397414
In order to find the activation energy, the found a and b will help us.
Doing the calculation for K =1.38064 × 10^{-23} m^2 kg s^{-2} K^{-1}: and A = 1.44588 average pixel count/s.

4. UNCERTAINTY IN THE SIGNAL

i. Temperature Dependent Biases

Temperature [°C]	**2**	**5**	**8**	**11**	**15**	**17**	**20**
Uncertainty	6.89034	7.27570	7.03217	7.05606	7.65657	8.31522	9.12840

ii. Time Dependent Darks

Temperature [°C]	**5**	**10**	**20**	**40**	**80**	**160**
Uncertainty	10.71800	17.05573	14.21642	12.17817	15.32264	19.56825

iii. Temperature Dependent Darks

Temperature [°C]	**5**	**8**	**11**	**17**	**20**
Uncertainty	9.97484	11.47484	13.26983	16.42022	23.29525

4. CONCLUSION

Excluding biases, our data supports our initial assumptions with few outliers and the null hypotheses are not rejected. Darks seem to be growing exponentially with temperature as predicted by the Arrhenius equation and the linear fit of the time inverse and logarithm is satisfactory. Darks also increase with time and a linear fit seems to be both reasonable and sufficient. On the other hand, biases are showing some direct proportionality to temperature which can be explained because of the nonzero exposure time in practice. Nonetheless, the slope is still quite shallow.